

Adaptive Discontinuous Galerkin Finite Element Methods for the Compressible Euler Equations

Ralf Hartmann* and Paul Houston†

**Institute of Applied Mathematics, University of Heidelberg, Im Neuenheimer Feld 293, D-69120 Heidelberg, Germany; and †Department of Mathematics & Computer Science, University of Leicester, Leicester LE1 7RH, United Kingdom*

E-mail: Ralf.Hartmann@iwr.uni-heidelberg.de and Paul.Houston@mcs.le.ac.uk

Received January 2, 2002; revised July 23, 2002

In this paper a recently developed approach for the design of adaptive discontinuous Galerkin finite element methods is applied to physically relevant problems arising in inviscid compressible fluid flows governed by the Euler equations of gas dynamics. In particular, we employ (weighted) type I *a posteriori* bounds to drive adaptive finite element algorithms for the estimation of the error measured in terms of general target functionals of the solution; these error estimates involve the product of the finite element residuals with local weighting terms, involving the solution of a certain dual problem that must be numerically approximated. This general approach leads to the design of economical finite element meshes specifically tailored to the computation of the target functional of interest, as well as providing reliable and efficient error estimation. The superiority of the proposed approach over mesh refinement algorithms which employ standard unweighted (type II) error indicators, which do not require the solution of an auxiliary problem, are illustrated by a series of numerical experiments; here, we consider transonic flow through a nozzle, as well as subsonic and supersonic flows around different airfoil geometries. © 2002 Elsevier Science (USA)

Key Words: discontinuous Galerkin method; *a posteriori* error analysis; adaptivity; compressible Euler equations.

1. INTRODUCTION

One of the main challenges in the field of computational partial differential equations is the design and implementation of efficient adaptive finite element/finite volume methods which approximate the solution to complex multidimensional problems with guaranteed error control. While for problems arising in solid mechanics several software packages exist which are capable of achieving this goal, for fluid flow problems involving partial differential equations of hyperbolic/nearly hyperbolic character, the situation is far less

advanced. Indeed, the majority of adaptive CFD algorithms will refine or adjust the computational grid according to an empirical criterion, such as a large gradient in one of the field variables. Although this intuitive approach has had some success, it does not provide practical and sharp error estimation. An alternative to this heuristic approach is to derive reliable and efficient *a posteriori* error bounds which can successfully drive adaptive algorithms; for a review of some of the main developments in this area we refer readers to the recent monographs [1, 26, 28] and the articles [6, 9, 10, 25].

The purpose of this paper is to apply the recently developed approach of weighted *a posteriori* error estimation for discontinuous Galerkin finite element methods (see [14, 16]) to the discretisation of physically relevant problems arising in inviscid compressible fluid flows governed by the Euler equations of gas dynamics; for related work, we refer readers to [3, 5, 11, 17, 21–24, 27], for example. Here, by employing a hyperbolic duality argument, weighted or type I (cf. [18]) *a posteriori* error bounds for general functionals of the solution of practical relevance may be derived; typical examples include the drag and lift coefficients of a body immersed in an inviscid fluid, the local mean value of the field or its flux through the outflow boundary of the computational domain, and the pointwise evaluation of a component of the solution vector at a given point in the computational domain. In these type I error estimates the element-residuals are multiplied by local weights involving the solution of a certain dual problem. These weights provide invaluable information concerning the global transport of the error and the interaction of the error in different components of the solution. The elimination of these weights gives rise to traditional type II *a posteriori* error bounds (cf. [9, 11]), for example; in practice, these unweighted error estimates lead to the design of inefficient adaptive computational meshes. In this article we consider the performance of weighted *a posteriori* error indicators for both interior and exterior inviscid compressible flows of practical interest. In particular, we demonstrate the superiority of the proposed approach over mesh refinement algorithms which employ standard type II error indicators: weighted *a posteriori* error estimates lead to the design of economical finite element meshes specifically tailored to the computation of the target functional of interest, as well as providing reliable and efficient error estimation.

The outline of this paper is as follows. In order to highlight the key ideas pursued in this paper, in Section 2 we present an overview of duality-based *a posteriori* error estimation. In Section 3 we introduce the compressible Euler equations of gas dynamics and formulate their discontinuous Galerkin finite element approximation. Then, in Section 4 we derive *a posteriori* error bounds for general linear and nonlinear functionals of the solution based on the approach outlined in Section 2 (cf. [14, 16]). The performance of the proposed type I *a posteriori* error estimator is then studied in Section 5 through a series of numerical experiments; here, we consider transonic flow through a nozzle, as well as subsonic and supersonic flows around different airfoil geometries. In particular, we demonstrate the superiority of using our weighted *a posteriori* error indicators over traditional error indicators which do not require the solution of an auxiliary or dual problem. Finally, in Section 6 we summarise the work presented in this paper and draw some conclusions.

2. A PARADIGM FOR A POSTERIORI ERROR ESTIMATION

In this section we present an overview of the general theoretical framework of duality-based *a posteriori* error estimation developed by C. Johnson and R. Rannacher and their

collaborators. For a detailed discussion, we refer readers to the series of articles [5, 6, 9–11, 17, 24, 25] and references therein.

Let X and Y be two Hilbert spaces. Further, we write $\mathcal{N}(\cdot, \cdot)$ to denote a semilinear form (nonlinear in its first argument, but linear in its second), with Fréchet derivative $\mathcal{N}'[\cdot](\cdot, \cdot)$. We suppose that u is the unique solution to the variational problem: find u in X such that

$$\mathcal{N}(u, v) = 0, \quad \forall v \in Y. \quad (1)$$

Problem (1) can be thought of as the weak formulation of a nonlinear partial differential equation on X whose unique solution is $u \in X$. In practice (1) cannot be solved in closed form but needs to be approximated numerically. For the purposes of this paper, we only consider an h -version finite element approximated to (1); for the extension to general hp -adaptive methods, we refer readers to the articles [18, 25] and references therein. In order to construct a Galerkin approximation to this problem, we consider a sequence of finite-dimensional spaces $\{X_h\}$, parameterised by the positive discretisation parameter h ; for the sake of simplicity we suppose that $X_h \subset X$ for each h . Simultaneously, consider a sequence of finite-dimensional spaces $\{Y_h\}$, with Y_h contained in Y for each h . For the purposes of this paper, X_h and Y_h can be thought of as finite element spaces consisting of piecewise polynomial functions on a partition \mathcal{T}_h , of granularity h , of the computational domain. The Galerkin approximation u_h of u is then sought in X_h as the solution of the finite-dimensional problem

$$\mathcal{N}(u_h, v_h) = 0, \quad \forall v_h \in Y_h. \quad (2)$$

For simplicity of presentation, we assume that X_h and Y_h are suitably chosen finite element spaces to ensure the existence of a unique solution u_h to (2).

In many problems of physical importance the quantities of interest may be a series of target or error functionals $J_i(\cdot)$, $i = 1, \dots, N$, $N \geq 1$, of the solution. Relevant examples include the mean flow across a line, the point value of the solution, and the drag and lift coefficients of a body immersed in an inviscid fluid. For simplicity, we restrict ourselves to the case of a single target functional, i.e., $N = 1$, and write $J(\cdot) \equiv J_1(\cdot)$; for the extension of the proceeding theory to multiple target functionals, see [15]. In order to obtain a computable *a posteriori* bound on the error between the true value of the functional $J(u)$ and the computed value $J(u_h)$, we begin by noting the Galerkin orthogonality of the discretisation (2):

$$\mathcal{N}(u, v_h) - \mathcal{N}(u_h, v_h) = 0, \quad \forall v_h \in Y_h. \quad (3)$$

This will be a key ingredient in the following *a posteriori* error analysis. Additionally, let us introduce some notation. Assuming that the functional of interest $J(\cdot)$ defined on X is differentiable, we write $\bar{J}(\cdot, \cdot; \cdot)$ to denote the mean value linearisation of $J(\cdot)$ defined by

$$\bar{J}(u, u_h; u - u_h) = J(u) - J(u_h) = \int_0^1 J'[\theta u + (1 - \theta)u_h](u - u_h) d\theta, \quad (4)$$

where $J'[w](\cdot)$ denotes the Fréchet derivative of $J(\cdot)$ evaluated at some w in X .

Analogously, we write $\mathcal{M}(u, u_h; \cdot, \cdot)$ to denote the mean-value linearisation of the semi-linear form $\mathcal{N}(\cdot, \cdot)$ given by

$$\begin{aligned}\mathcal{M}(u, u_h; u - u_h, v) &= \mathcal{N}(u, v) - \mathcal{N}(u_h, v) \\ &= \int_0^1 \mathcal{N}'[\theta u + (1 - \theta)u_h](u - u_h, v) d\theta\end{aligned}\quad (5)$$

for all v in Y . With this notation, we note that the Galerkin orthogonality property (3) may be expressed in the form

$$\mathcal{M}(u, u_h; u - u_h, v_h) = 0, \quad \forall v_h \in Y_h. \quad (6)$$

We now introduce the following *dual* or *adjoint* problem: find $z \in Y$ such that

$$\mathcal{M}(u, u_h; w, z) = \bar{J}(u, u_h; w), \quad \forall w \in X. \quad (7)$$

We assume that (7) possesses a unique solution. Clearly, the validity of this assumption depends on both the definition of $\mathcal{M}(u, u_h; \cdot, \cdot)$ and the choice of the functional under consideration. Important examples which are covered by our hypothesis are discussed in [14, 18].

For the proceeding error analysis, we must therefore *assume* that the dual problem (7) is well posed. Under this assumption, employing the Galerkin orthogonality property (6) we deduce the error representation formula

$$\begin{aligned}J(u) - J(u_h) &= \bar{J}(u, u_h; u - u_h) = \mathcal{M}(u, u_h; u - u_h, z) \\ &= \mathcal{M}(u, u_h; u - u_h, z - z_h) = -\mathcal{N}(u_h, z - z_h)\end{aligned}\quad (8)$$

for all z_h in the finite element space Y_h . On the basis of the general error representation formula (8), *a posteriori* estimates which provide upper bounds on the true error in the computed target functional $J(\cdot)$ may be deduced. The simplest approach is to first decompose the right-hand side of (8) as a summation of local error indicators $\eta_{\kappa}^{(1)}$ over the elements κ in the computational mesh \mathcal{T}_h ; i.e., we write

$$J(u) - J(u_h) = -\mathcal{N}(u_h, z - z_h) \equiv \mathcal{E}_{\Omega}^{(1)}(u, u_h, h, z - z_h) = \sum_{\kappa \in \mathcal{T}_h} \eta_{\kappa}^{(1)}.$$

Then, on application of the triangle inequality, we deduce the following weighted or type I *a posteriori* error bound.

THEOREM 1. *Let u and u_h denote the solutions of (1) and (2), respectively, and suppose that the dual problem (7) is well posed. Then, the following type I *a posteriori* error bound holds:*

$$|J(u) - J(u_h)| \leq \mathcal{E}_{|\Omega|}^{(1)}(u, u_h, h, z - z_h) \equiv \sum_{\kappa \in \mathcal{T}_h} |\eta_{\kappa}^{(1)}|. \quad (9)$$

We remark that the local error indicators $\eta_{\kappa}^{(1)}$ appearing on the right-hand side of (9) involve the multiplication of finite element *residuals* depending only on u_h , with local

weighting terms involving the difference between the dual solution z satisfying (7) and its projection/interpolant z_h onto the finite element space Y_h ; in Section 4, we provide a concrete example arising from the discontinuous Galerkin approximation of the two-dimensional steady-state compressible Euler equations of gas dynamics. These weights represent the sensitivity of the error in the target functional $J(\cdot)$ with respect to variations of the local element residuals. Since the solution to the dual problem is usually unknown analytically, it may be desirable to eliminate z from (9); indeed, by employing the Cauchy–Schwarz inequality, together with standard results from approximation theory, the right-hand side of (9) may be bounded from above in terms of powers of the mesh function h and Sobolev seminorms of z . For then, finally, z may be completely eliminated from the *a posteriori* estimate by bounding norms of z by suitable norms of the data for the dual problem (7) by employing well-posed results. The resulting type II (cf. [18]) *a posteriori* error bound now only involves the computable finite element residuals, the discretisation parameter h , interpolation constants, and the stability factor for the dual problem. Thereby, a type II *a posteriori* error bound may be expressed in the general form

$$|J(u) - J(u_h)| \leq \mathcal{E}_{|\Omega|}^{(\text{II})}(u, u_h, h),$$

where the upper bound $\mathcal{E}_{|\Omega|}^{(\text{II})}(u, u_h, h)$ depends on certain norms involving the finite element residuals multiplied by an interpolation constant C_{int} and the stability factor C_{stab} of the dual problem (cf. [9, 11, 14, 18]), for example. These types of bounds are in the spirit of the ones derived by C. Johnson and his co-workers.

We stress that both type I and type II *a posteriori* estimates provide upper bounds on the error in the computed target functional. Moreover, each type of bound requires the numerical approximation of the dual problem (7); in the case of the type I estimate an approximation \hat{z} to z must be inserted into the right-hand side of (9) in order to evaluate the bound, while the type II bound requires knowledge of the stability factor C_{stab} . We remark that while C_{stab} may be determined from an analytical study of the well posedness of the dual problem, typically such general arguments lead to a considerable overestimate of C_{stab} ; thereby, in practice the stability factor C_{stab} must be determined computationally. This involves numerically approximating the dual solution for a large set of “typical” data—a task that is computationally much more demanding than solving a single dual problem for a type I error bound. While the resulting stability factor is applicable to all problems “covered” by the set of typical data, the resulting type II bound may still largely overestimate the error in a specific problem of practical interest.

Therefore, the computation of the dual solution, for use in a type I error bound, may pay off by leading to considerably sharper error estimates and the production of computational meshes, which are more economical than those stemming from a type II *a posteriori* error bound. Indeed, we shall see in Section 5 that the elimination of the weighting terms involving the difference between the dual solution z and z_h may adversely affect the efficiency of the resulting adaptive algorithm, leading to uneconomical mesh design (cf. [5, 14, 16, 17, 24]).

As a final remark, we note that before the dual solution z can be approximated numerically, the dependence of the data arising in the definition of the auxiliary problem (7) on the true solution u to the original (primal) *nonlinear* partial differential equation (1) must be eliminated. To this end, in practice, the linearisations $\bar{J}(u, u_h; \cdot)$ and $\mathcal{M}(u, u_h; \cdot, \cdot)$ of $\mathcal{N}(\cdot, \cdot)$ and $J(\cdot)$, respectively, are approximated by $\bar{J}(u_h, u_h; \cdot)$ and $\mathcal{M}(u_h, u_h; \cdot, \cdot)$, respectively; quantifying the size of these approximations is a rather delicate task and depends on the

particular problem under consideration. We shall return to these issues concerning the linearisation of $\mathcal{N}(\cdot, \cdot)$ and $J(\cdot)$ and the numerical approximation of the dual problem (7) in Section 4, when we consider the discontinuous Galerkin approximation to the inviscid compressible Euler equations of gas dynamics.

Remark 1. We note that the above theory of *a posteriori* error estimation holds for both steady and unsteady partial differential equations discretised within the Galerkin framework. However, for time-dependent problems there are still many outstanding issues concerning the computational implementation and efficiency of the proposed approach, particularly for nonlinear problems; for related work, see Bangerth and Rannacher [2] and Harriman [12], for example.

3. MODEL PROBLEM AND DISCRETISATION

We consider the two-dimensional steady-state compressible Euler equations of gas dynamics. Writing ρ , (u, v) , p , and E to denote the density, Cartesian velocity, pressure, and total energy per unit mass, respectively, the equations of motion are given by

$$\operatorname{div} \mathcal{F}(\mathbf{u}) \equiv \sum_{i=1}^2 \frac{\partial}{\partial x_i} \mathbf{f}_i(\mathbf{u}) = 0 \quad \text{in } \Omega, \quad (10)$$

where Ω is an open bounded domain in \mathbb{R}^2 . Here, the vector of conservative variables \mathbf{u} and the fluxes \mathbf{f}_i , $i = 1, 2$, are defined by $\mathbf{u} = (\rho, \rho u, \rho v, \rho E)$, $\mathbf{f}_1 = (\rho u, \rho u^2 + p, \rho uv, \rho Hu)$, and $\mathbf{f}_2 = (\rho v, \rho uv, \rho v^2 + p, \rho Hv)$, respectively. Additionally, H is the total enthalpy defined by $H = E + p/\rho$. The equation of state of an ideal gas is given by $p = (\gamma - 1)\rho(E - (u^2 + v^2)/2)$, where γ is the ratio of specific heats, which, for dry air, is $\gamma = 1.4$.

If the analytical solution \mathbf{u} is sufficiently smooth, then (10) may be written in the non-conservative quasilinear form

$$\sum_{i=1}^2 A_i(\mathbf{u}) \frac{\partial \mathbf{u}}{\partial x_i} = 0, \quad \text{in } \Omega,$$

where $A_i(\mathbf{u}) := \nabla_{\mathbf{u}} \mathbf{f}_i(\mathbf{u})$ denote the Jacobi matrices of the fluxes $\mathbf{f}_i(\mathbf{u})$, $i = 1, 2$. Thereby,

$$A_1(\mathbf{u}) = \begin{bmatrix} 0 & 1 & 0 & 0 \\ \frac{\gamma-3}{2}u^2 + \frac{\gamma-1}{2}v^2 & (3-\gamma)u & (1-\gamma)v & \gamma-1 \\ -uv & v & u & 0 \\ (\gamma-1)u(u^2+v^2) - \gamma u E & \gamma E - \frac{\gamma-1}{2}(v^2+3u^2) & (1-\gamma)uv & \gamma u \end{bmatrix}$$

and

$$A_2(\mathbf{u}) = \begin{bmatrix} 0 & 0 & 1 & 0 \\ -uv & v & u & 0 \\ \frac{\gamma-3}{2}v^2 + \frac{\gamma-1}{2}u^2 & (1-\gamma)u & (3-\gamma)v & \gamma-1 \\ (\gamma-1)v(u^2+v^2) - \gamma v E & (1-\gamma)uv & \gamma E - \frac{\gamma-1}{2}(u^2+3v^2) & \gamma v \end{bmatrix}.$$

Given that $\Omega \subset \mathbb{R}^2$ is a bounded region, with boundary Γ , the system of conservation laws (10) must be supplemented by appropriate boundary conditions; for example, at inflow/outflow boundaries, we require that

$$A^-(\mathbf{u}, \mathbf{n})(\mathbf{u} - \mathbf{g}) = \mathbf{0}, \quad (11)$$

where \mathbf{n} denotes the unit outward normal vector to the boundary Γ and \mathbf{g} is a (given) real-valued vector function. Here, $A^-(\mathbf{u}, \mathbf{n})$ denotes the negative part of $A(\mathbf{u}, \mathbf{n}) := \sum_{i=1}^2 \mathbf{n}_i A_i(\mathbf{u})$; i.e., $A^-(\mathbf{u}, \mathbf{n}) = R\Lambda^-L$, where L and R denote the 4×4 matrices of left and right eigenvectors of $A(\mathbf{u}, \mathbf{n})$, respectively, and $\Lambda^- = \text{diag}(\min(\lambda_i, 0))$ the 4×4 diagonal matrix of the negative eigenvalues of $A(\mathbf{u}, \mathbf{n})$.

In order to formulate the discontinuous Galerkin finite element approximation to (10), we first begin by introducing the necessary notation. Suppose that $l \geq 1$, and that \mathcal{T}_h is a regular or l -irregular subdivision of Ω into open-element domains κ such that $\bar{\Omega} = \bigcup_{\kappa \in \mathcal{T}_h} \bar{\kappa}$, where $\bar{\kappa}$ denotes the closure of κ . Thus, an edge of each element κ in \mathcal{T}_h is allowed to contain at most l hanging (irregular) nodes; when $l = 1$, the hanging node is typically the barycenter of the edge. Here, h denotes the piecewise constant mesh function defined by $h|_{\kappa} \equiv h_{\kappa} = \text{diam}(\kappa)$ for all $\kappa \in \mathcal{T}_h$. We shall suppose that the family of subdivisions \mathcal{T}_h is shape regular and that each $\kappa \in \mathcal{T}_h$ is a smooth bijective image of a fixed reference element $\hat{\kappa}$; that is, $\kappa = F_{\kappa}(\hat{\kappa})$ for all $\kappa \in \mathcal{T}_h$, where $\hat{\kappa}$ is either the open-unit simplex (triangle in two dimensions) or the open-unit square $(0, 1)^2$ in \mathbb{R}^2 . On the reference element $\hat{\kappa}$ we define spaces of polynomials of degree $p \geq 0$ as follows:

$$\mathcal{Q}_p = \text{span}\{\hat{\mathbf{x}}^{\alpha} : 0 \leq \alpha_i \leq p, 0 \leq i \leq 2\},$$

$$\mathcal{P}_p = \text{span}\{\hat{\mathbf{x}}^{\alpha} : 0 \leq |\alpha| \leq p\}.$$

We now introduce the finite element space $S_{h,p}$ consisting of discontinuous vector (of dimension 4)-valued polynomial functions of degree $p \geq 0$, defined by

$$S_{h,p} = \begin{cases} \mathbf{v} \in [L_2(\Omega)]^4 : \mathbf{v}|_{\kappa} \circ F_{\kappa} \in [\mathcal{Q}_p]^4, & \text{if } \hat{\kappa} = F_{\kappa}^{-1}(\kappa) \text{ is the square } (0, 1)^2, \\ \mathbf{v}|_{\kappa} \circ F_{\kappa} \in [\mathcal{P}_p]^4, & \text{if } \hat{\kappa} = F_{\kappa}^{-1}(\kappa) \text{ is the unit simplex; } \kappa \in \mathcal{T}_h. \end{cases}$$

For each $\kappa \in \mathcal{T}_h$ and any $v \in H^1(\kappa)$ we denote by v^+ the interior trace of v on $\partial\kappa$ (the trace taken from within κ). Now consider an element κ such that the set $\partial\kappa \setminus \Gamma$ is nonempty; then, for each $x \in \partial\kappa \setminus \Gamma$ (with the exception of a set of one-dimensional measure zero) there exists a unique element κ' , depending on the choice of x , such that $x \in \partial\kappa'$. This is illustrated in Fig. 1. Now suppose that $v \in H^1(\kappa)$ for each $\kappa \in \mathcal{T}_h$. If $\partial\kappa \setminus \Gamma$ is nonempty for some $\kappa \in \mathcal{T}_h$, then we can also define the outer trace v^- of v on $\partial\kappa \setminus \Gamma$ relative to κ as the inner trace v^+ relative to those elements κ' for which $\partial\kappa'$ has intersection with $\partial\kappa \setminus \Gamma$ of positive one-dimensional measure.

To formulate the discontinuous Galerkin method, we first introduce a weak formulation of (10). To this end, we multiply the conservation law (10) by an arbitrary smooth function \mathbf{v} and integrate by parts over an element κ in the mesh \mathcal{T}_h ; thereby, we get

$$-\int_{\kappa} \mathcal{F}(\mathbf{u}) \cdot \nabla \mathbf{v} \, d\mathbf{x} + \int_{\partial\kappa} \mathcal{F}(\mathbf{u}^+) \cdot \mathbf{n}_{\kappa} \mathbf{v}^+ \, ds = 0, \quad (12)$$

where \mathbf{n}_{κ} denotes the unit outward normal vector to $\partial\kappa$.

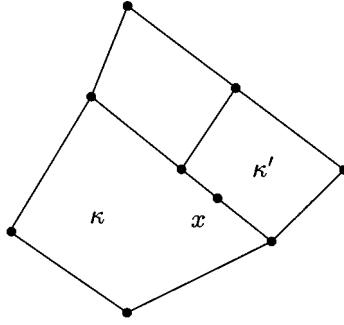


FIG. 1. A point x such that $x \in \partial\kappa$ and $x \in \partial\kappa'$.

To discretise (12), we replace the analytical solution \mathbf{u} with the Galerkin finite element approximation \mathbf{u}_h and the test function \mathbf{v} with \mathbf{v}_h , where \mathbf{u}_h and \mathbf{v}_h both belong to the finite element space $S_{h,p}$. In addition, since the numerical solution \mathbf{u}_h is discontinuous between element interfaces, we must replace the flux $\mathcal{F}(\mathbf{u}^+) \cdot \mathbf{n}_\kappa$ with a *numerical flux* function $\mathcal{H}(\mathbf{u}_h^+, \mathbf{u}_h^-, \mathbf{n}_\kappa)$, which depends on both the inner and outer trace of \mathbf{u}_h on $\partial\kappa$, $\kappa \in \mathcal{T}_h$, and the unit outward normal vector \mathbf{n}_κ to $\partial\kappa$. Furthermore, to suppress the generation of nonphysical oscillations, we add an artificial viscosity/shock-capture term which depends on both the mesh function h and the finite element residual. Thereby, summing over the elements κ in the mesh \mathcal{T}_h yields the following discontinuous Galerkin finite element discretisation of (10): find $\mathbf{u}_h \in S_{h,p}$ such that

$$\begin{aligned} \mathcal{N}(\mathbf{u}_h, \mathbf{v}_h) \equiv & \sum_{\kappa \in \mathcal{T}_h} \left\{ - \int_{\kappa} \mathcal{F}(\mathbf{u}_h) \cdot \nabla \mathbf{v}_h \, d\mathbf{x} + \int_{\partial\kappa} \mathcal{H}(\mathbf{u}_h^+, \mathbf{u}_h^-, \mathbf{n}_\kappa) \mathbf{v}_h^+ \, ds \right. \\ & \left. + \int_{\kappa} \varepsilon \nabla \mathbf{u}_h \cdot \nabla \mathbf{v}_h \, d\mathbf{x} \right\} = 0 \quad \forall \mathbf{v}_h \in S_{h,p}. \end{aligned} \quad (43)$$

$\nabla \mathbf{u}_h = \begin{pmatrix} \frac{\partial u_1}{\partial x} & \frac{\partial u_1^2}{\partial x} & \frac{\partial u_1^3}{\partial x} & \frac{\partial u_1^4}{\partial x} \\ \frac{\partial u_1}{\partial y} & \frac{\partial u_1^2}{\partial y} & \frac{\partial u_1^3}{\partial y} & \frac{\partial u_1^4}{\partial y} \end{pmatrix}$

Here, ε denotes the artificial viscosity coefficient matrix defined by

$$\varepsilon = C_\varepsilon h^{2-\beta} |\operatorname{div} \mathcal{F}(\mathbf{u}_h)| I, \quad \varepsilon = \begin{pmatrix} \varepsilon & \\ & \varepsilon \end{pmatrix} \quad (14)$$

where C_ε and $0 < \beta < 1/2$ are positive constants and I denotes the identity matrix in \mathbb{R}^2 . The definition of ε in (14) represents a slight modification of the artificial viscosity model introduced and analysed by Jaffre *et al.* [19]; for related work, we refer readers to [4, 8], for example.

Remark 2. For elements $\kappa \in \mathcal{T}_h$ whose boundary intersects that of the computational domain Ω , we replace \mathbf{u}_h^- with appropriate boundary conditions on the portion of $\partial\kappa$ for which $\partial\kappa \cap \Gamma \neq \emptyset$. At inflow/outflow boundaries, the state \mathbf{u}_h^- is determined via a local characteristic decomposition of the incoming and outgoing waves in the direction normal to the boundary (cf. (11)). At solid walls, a symmetry technique is employed; here, \mathbf{u}_h^- has the same density, total energy, and *tangential* velocity as \mathbf{u}_h^+ , but \mathbf{u}_h^- is assigned the opposite *normal* velocity to \mathbf{u}_h^+ (cf. [4]).

We note that the replacement of the flux $\mathcal{F}(\mathbf{u}^+) \cdot \mathbf{n}_\kappa$ with the numerical flux function $\mathcal{H}(\mathbf{u}_h^+, \mathbf{u}_h^-, \mathbf{n}_\kappa)$ on the boundary of element κ , $\kappa \in \mathcal{T}_h$, corresponds to the weak imposition of the boundary data (cf. [4]). Furthermore, we emphasise the fact that the choice of the

numerical flux function is *independent* of the finite element space employed. Indeed, the numerical flux $\mathcal{H}(\cdot, \cdot, \cdot)$ may be chosen to be any two-point monotonic Lipschitz function which satisfies the following two conditions:

- (i) $\mathcal{H}(\cdot, \cdot, \cdot)|_{\partial\kappa}$ is consistent with $\mathcal{F}(\cdot) \cdot \mathbf{n}_\kappa$ for each κ in \mathcal{T}_h ; i.e., $\mathcal{H}(\mathbf{u}, \mathbf{u}, \mathbf{n}_\kappa)|_{\partial\kappa} = \mathcal{F}(\mathbf{u}) \cdot \mathbf{n}_\kappa$ for all κ in \mathcal{T}_h ;
- (ii) $\mathcal{H}(\cdot, \cdot, \cdot)$ is conservative; i.e., given any two neighbouring elements κ and κ' from the finite element partition \mathcal{T}_h , at each point $\mathbf{x} \in \partial\kappa \cap \partial\kappa' \neq \emptyset$, noting that $\mathbf{n}_{\kappa'} = -\mathbf{n}_\kappa$, we have that $\mathcal{H}(\mathbf{v}, \mathbf{w}, \mathbf{n}_\kappa) = -\mathcal{H}(\mathbf{w}, \mathbf{v}, -\mathbf{n}_\kappa)$.

There are several numerical flux functions satisfying these conditions, such as the Godunov flux, the Engquist–Osher flux, the Roe flux, and the Vijayasundaram flux, for example (cf. Kröner [20] and references therein). In Section 5, we employ the (local) Lax–Friedrichs flux $\mathcal{H}_{LF}(\cdot, \cdot, \cdot)$ defined by

$$\mathcal{H}_{LF}(\mathbf{u}_h^+, \mathbf{u}_h^-, \mathbf{n}_\kappa)|_{\partial\kappa} = \frac{1}{2}(\mathcal{F}(\mathbf{u}_h^+) \cdot \mathbf{n}_\kappa + \mathcal{F}(\mathbf{u}_h^-) \cdot \mathbf{n}_\kappa - \alpha(\mathbf{u}_h^- - \mathbf{u}_h^+)), \quad (15)$$

for κ in \mathcal{T}_h , where α is an estimate of the largest eigenvalue (in absolute value) of the Jacobi matrix $A(\mathbf{u}_h, \mathbf{n}_\kappa)$ in the neighbourhood of $\partial\kappa$.

Remark 3. We note that the integrals involving the numerical flux function along the boundary $\partial\kappa$ of each element κ in the mesh \mathcal{T}_h arising in (13) are calculated by writing

$$\int_{\partial\kappa} \mathcal{H}(\mathbf{u}_h^+, \mathbf{u}_h^-, \mathbf{n}_\kappa) \mathbf{v}_h^+ \, ds = \sum_{e \subset \partial\kappa} \int_e \mathcal{H}(\mathbf{u}_h^+, \mathbf{u}_h^-, \mathbf{n}_\kappa) \mathbf{v}_h^+ \, ds,$$

where each open-edge $e \subset \partial\kappa$ is either the smallest common one-dimensional interface of neighbouring elements or a boundary edge of $\partial\kappa \cap \Gamma$. With this notation, hanging nodes can easily be handled, since they cannot arise in the interior of any edge $e \subset \partial\kappa$; i.e., each e is regular.

Assuming that the analytical solution \mathbf{u} to (10) is sufficiently smooth, then the Galerkin orthogonality property of the finite element method (13) is given by

$$\mathcal{N}(\mathbf{u}, \mathbf{v}_h) - \mathcal{N}(\mathbf{u}_h, \mathbf{v}_h) = 0, \quad \forall \mathbf{v}_h \in S_{h,p}; \quad (16)$$

here, we have employed the consistency condition (i) of the numerical flux function $\mathcal{H}(\cdot, \cdot, \cdot)$ and the consistency of the artificial viscosity terms.

4. A POSTERIORI ERROR ANALYSIS

Suppose that $\text{TOL} > 0$ is a prescribed tolerance and $J(\cdot)$ is a given target functional. In this section, we consider the measurement problem concerned with computing a numerical approximation \mathbf{u}_h from $S_{h,p}$ such that

$$|J(\mathbf{u}) - J(\mathbf{u}_h)| \leq \text{TOL}. \quad (17)$$

To this end, based on the general framework of a *posteriori* error estimation developed in Section 2, we proceed by deriving a computable upper bound on the error between $J(\mathbf{u})$ and $J(\mathbf{u}_h)$; for a more detailed account, we refer readers to the article [14].

Recalling the notation introduced in Section 2, we define the following dual or adjoint problem: find $\mathbf{z} \in V$ such that

$$\mathcal{M}(\mathbf{u}, \mathbf{u}_h; \mathbf{w}, \mathbf{z}) = \bar{J}(\mathbf{u}, \mathbf{u}_h; \mathbf{w}), \quad \forall \mathbf{w} \in V, \quad (18)$$

where V is some suitably chosen function space such that $S_{h,p} \subset V$. Here, we write $\mathcal{M}(\mathbf{u}, \mathbf{u}; \cdot, \cdot)$ to denote the mean-value linearisation of the semilinear form $\mathcal{N}(\cdot, \cdot)$ introduced in (5), where $\mathcal{N}(\cdot, \cdot)$ is defined in Section 3 (cf. (13)). We remark that the linearisation defined in (5) is only a *formal* calculation, in the sense that $\mathcal{N}'[\mathbf{w}](\cdot, \mathbf{v})$ may not in general exist. Instead, a suitable approximation to $\mathcal{N}'[\mathbf{w}](\cdot, \mathbf{v})$ in the direction $\mathbf{u} - \mathbf{u}_h$ must be determined, for example, by computing appropriate finite difference quotients of $\mathcal{N}(\cdot, \mathbf{v})$ (cf. [14]). For the purposes of the proceeding analysis, we *assume* that the linearisation performed in (5), with $\mathcal{N}(\cdot, \cdot)$ defined by (13), is well defined. Moreover, as in Section 2, we assume that (18) is a well-posed problem. Under these assumptions, we have the following general result.

THEOREM 2. *Let \mathbf{u} and \mathbf{u}_h denote the solutions of (10) and (13), respectively, and suppose that the dual problem (18) is well posed. Then, the error representation formula*

$$J(\mathbf{u}) - J(\mathbf{u}_h) = \mathcal{E}_\Omega^{(1)}(\mathbf{u}, \mathbf{u}_h, h, \mathbf{z} - \mathbf{z}_h) \equiv \sum_{\kappa \in \mathcal{T}_h} \eta_\kappa^{(1)}, \quad (19)$$

where

$$\eta_\kappa^{(1)} = \int_\kappa R_h(\mathbf{z} - \mathbf{z}_h) d\mathbf{x} + \int_{\partial\kappa} r_h(\mathbf{z} - \mathbf{z}_h)^+ ds - \int_\kappa \varepsilon \nabla \mathbf{u}_h \cdot \nabla(\mathbf{z} - \mathbf{z}_h) d\mathbf{x} \quad (20)$$

for all \mathbf{z}_h in $S_{h,p}$, holds. Here, R_h and r_h denote the internal and boundary finite element residuals, respectively, defined on $\kappa \in \mathcal{T}_h$ by

$$R_h|_\kappa = -\operatorname{div} \mathcal{F}(\mathbf{u}_h) \quad \text{and} \quad r_h|_\kappa = \mathcal{F}(\mathbf{u}_h^+) \cdot \mathbf{n}_\kappa - \mathcal{H}(\mathbf{u}_h^+, \mathbf{u}_h^-, \mathbf{n}_\kappa), \quad (21)$$

respectively.

Proof. Choosing $\mathbf{w} = \mathbf{u} - \mathbf{u}_h$ in (18), recalling the linearisation performed in (4), and exploiting the Galerkin orthogonality property (16), we deduce that

$$J(\mathbf{u}) - J(\mathbf{u}_h) = -\mathcal{N}(\mathbf{u}_h, \mathbf{z} - \mathbf{z}_h)$$

for all \mathbf{z}_h in $S_{h,p}$ (cf. (8)). Employing the divergence theorem, we have that

$$\begin{aligned} J(\mathbf{u}) - J(\mathbf{u}_h) &= \sum_{\kappa \in \mathcal{T}_h} \left\{ - \int_\kappa \operatorname{div} \mathcal{F}(\mathbf{u}_h)(\mathbf{z} - \mathbf{z}_h) d\mathbf{x} + \int_{\partial\kappa} (\mathcal{F}(\mathbf{u}_h^+) \cdot \mathbf{n}_\kappa - \mathcal{H}(\mathbf{u}_h^+, \mathbf{u}_h^-, \mathbf{n}_\kappa)) \right. \\ &\quad \left. \times (\mathbf{z} - \mathbf{z}_h)^+ ds - \int_\kappa \varepsilon \nabla \mathbf{u}_h \cdot \nabla(\mathbf{z} - \mathbf{z}_h) d\mathbf{x} \right\}. \end{aligned} \quad (22)$$

Using the definition of the residuals R_h and r_h in (21), gives the desired result. ■

The measurement problem (17) is equivalent to demanding that the *stopping criterion*

$$|\mathcal{E}_\Omega^{(1)}(\mathbf{u}, \mathbf{u}_h, h, \mathbf{z} - \mathbf{z}_h)| \leq \text{TOL} \quad (23)$$

be satisfied (cf. Eq. (19)). As it stands, the left-hand side of (23) is not “computable” since it involves the unknown analytical solutions \mathbf{u} and \mathbf{z} to the primal and dual problems (10) and (18), respectively. As noted in Section 2, the dependence of the error representation formula (19) on \mathbf{u} stems from the linearisations of $\mathcal{N}(\cdot, \cdot)$ and $J(\cdot)$ performed in (5) and (4), respectively.

In practice, the linearisations leading to $\mathcal{M}(\mathbf{u}, \mathbf{u}_h; \cdot, \cdot)$ and $\bar{J}(\mathbf{u}, \mathbf{u}_h; \cdot)$ are performed about \mathbf{u}_h and the dual solution \mathbf{z} is approximated by a discontinuous Galerkin approximation $\hat{\mathbf{z}}$ computed on a sequence of suitable “dual” finite element spaces $S_{\hat{h}, \hat{p}}$, based on a “dual” partition $\mathcal{T}_{\hat{h}}$ and “dual” polynomial degree \hat{p} , which may differ from the “primal” partition \mathcal{T}_h and “primal” polynomial degree p , respectively. Further, \mathbf{z}_h will denote the $L_2(\Omega)$ orthogonal projection of the numerically computed dual solution $\hat{\mathbf{z}}$ onto the primal finite element space $S_{h,p}$ defined over the primal subdivision \mathcal{T}_h .

Let us now replace \mathbf{z} with $\hat{\mathbf{z}}$ in η_κ and decompose the error representation formula (19) into terms which are computable; namely, those involving \mathbf{u}_h and the numerical approximation $\hat{\mathbf{z}}$ to the dual solution, and those that require the analytical solutions \mathbf{u} and \mathbf{z} to the primal and dual problems, respectively. Writing

$$\mathcal{E}_\Omega^{(1)}(\mathbf{u}, \mathbf{u}_h, h, \mathbf{z} - \mathbf{z}_h) = \mathcal{E}_\Omega^{(1)}(\mathbf{u}_h, \mathbf{u}_h, h, \hat{\mathbf{z}} - \mathbf{z}_h) + \mathcal{E}_\Omega^{(1)}(\mathbf{u}, \mathbf{u}_h, h, \mathbf{z} - \hat{\mathbf{z}}),$$

we deduce that

$$\begin{aligned} |J(\mathbf{u}) - J(\mathbf{u}_h)| &\leq \hat{\mathcal{E}}_{|\Omega|}^{(1)}(\mathbf{u}_h, \mathbf{u}_h, h, \hat{\mathbf{z}} - \mathbf{z}_h) + \mathcal{E}_D \\ &\equiv \sum_{\kappa \in \mathcal{T}_h} |\hat{\eta}_\kappa| + |\mathcal{E}_\Omega^{(1)}(\mathbf{u}, \mathbf{u}_h, h, \mathbf{z} - \hat{\mathbf{z}})|, \end{aligned} \quad (24)$$

where $\hat{\eta}_\kappa$ is defined analogously to η_κ (cf. (20)), with \mathbf{z} replaced by $\hat{\mathbf{z}}$. Hence, a sufficient condition for the validity of our original stopping criterion (23) is that

$$\hat{\mathcal{E}}_{|\Omega|}^{(1)}(\mathbf{u}_h, \mathbf{u}_h, h, \hat{\mathbf{z}} - \mathbf{z}_h) + \mathcal{E}_D \leq \text{TOL}. \quad (25)$$

We note that the fundamental difference between the terms $\hat{\mathcal{E}}_{|\Omega|}^{(1)}(\mathbf{u}_h, \mathbf{u}_h, h, \hat{\mathbf{z}} - \mathbf{z}_h)$ and \mathcal{E}_D is that in the former, the absolute value signs appear under the summation over the elements $\kappa \in \mathcal{T}_h$, while in the latter, the absolute value sign is outside the sum. It has been shown through numerical experiments in [18] (cf. also [13, 14, 16]) that with a suitable choice of the dual finite element space $S_{\hat{h}, \hat{p}}$, \mathcal{E}_D is typically an order of magnitude smaller than $\hat{\mathcal{E}}_{|\Omega|}^{(1)}(\mathbf{u}_h, \mathbf{u}_h, h, \hat{\mathbf{z}} - \mathbf{z}_h)$. Therefore, \mathcal{E}_D can be safely absorbed into $\hat{\mathcal{E}}_{|\Omega|}^{(1)}(\mathbf{u}_h, \mathbf{u}_h, h, \hat{\mathbf{z}} - \mathbf{z}_h)$ without compromising the reliability of the adaptive algorithm when the stopping criterion (23) is replaced by

$$\hat{\mathcal{E}}_{|\Omega|}^{(1)}(\mathbf{u}_h, \mathbf{u}_h, h, \hat{\mathbf{z}} - \mathbf{z}_h) \leq \text{TOL}. \quad (26)$$

A bound of the form

$$|J(\mathbf{u}) - J(\mathbf{u}_h)| \lesssim \hat{\mathcal{E}}_{|\Omega|}^{(1)}(\mathbf{u}_h, \mathbf{u}_h, h, \hat{\mathbf{z}} - \mathbf{z}_h) \equiv \sum_{\kappa \in \mathcal{T}_h} |\hat{\eta}_\kappa| \quad (27)$$

which explicitly involves the numerical solution $\hat{\mathbf{z}}$ to the dual problem (through $\hat{\eta}_\kappa$ defined above) is referred to as a type I (cf. [18]) *a posteriori* error bound.

For the purposes of this paper, we approximate the dual solution \mathbf{z} using a discontinuous Galerkin approximation $\hat{\mathbf{z}}$ computed on the same mesh \mathcal{T}_h used for \mathbf{u}_h , but with a higher degree polynomial; i.e., $\hat{\mathbf{z}} \in S_{h,\hat{p}}$, where $\hat{p} > p$. For full details concerning the construction of the dual problem, including both the linearisation about the numerical solution and the implementation of suitable boundary conditions, we refer readers to [13, 14]. Here, we shall show through numerical experimentation in Section 5 that the reliability of the (approximate) type I *a posteriori* error bound (27) is not compromised, in the sense that

$$\hat{\mathcal{E}}_{|\Omega|}^{(I)} \equiv \hat{\mathcal{E}}_{|\Omega|}^{(I)}(\mathbf{u}_h, \mathbf{u}_h, h, \hat{\mathbf{z}} - \mathbf{z}_h) = \sum_{\kappa \in \mathcal{T}_h} |\hat{\eta}_\kappa^{(I)}| \quad (28)$$

remains an asymptotic upper bound on the true error in the target functional $J(\cdot)$ as the finite element mesh \mathcal{T}_h is adaptively refined. In particular, we shall show that the ratio of the approximate error representation formula

$$\hat{\mathcal{E}}_{\Omega}^{(I)} \equiv \mathcal{E}_{\Omega}^{(I)}(\mathbf{u}_h, \mathbf{u}_h, h, \hat{\mathbf{z}} - \mathbf{z}_h) = \sum_{\kappa \in \mathcal{T}_h} \hat{\eta}_\kappa^{(I)} \quad (29)$$

and the true value $J(\mathbf{u}) - J(\mathbf{u}_h)$ is extremely close to one (cf. [14, 16, 17, 21]).

As a final note, we remark that a more conservative approach to terminating an adaptive refinement algorithm based on the stopping criterion (26) is to enforce the stricter condition

$$\hat{\mathcal{E}}_{|\Omega|}^{(I)}(\mathbf{u}_h, \mathbf{u}_h, h, \hat{\mathbf{z}} - \mathbf{z}_h) \leq \theta \text{ TOL},$$

where the parameter $0 < \theta < 1$ may be selected by the user. However, even if the (approximate) *a posteriori* error bound (27) should fail to remain an upper bound on the true error in the computed target functional $J(\cdot)$ when \mathbf{z} is replaced by $\hat{\mathbf{z}}$, then this approach still provides the necessary local information to ensure that economical meshes, specifically tailored to the approximation of the underlying functional $J(\cdot)$ of interest, are generated.

Remark 4. As an alternative to shock capture, Barth and Larson [3] have considered the extension of the above analysis to the case of the piecewise constant discontinuous Galerkin method (13), i.e., where $p = 0$ (which corresponds to the lowest order Godunov finite volume method), together with general elementwise p -order reconstruction functions.

5. NUMERICAL EXPERIMENTS

In this section we present some numerical examples to highlight the advantages of designing an adaptive finite element algorithm based on the (approximate) type I error indicators $|\hat{\eta}_\kappa^{(I)}|$ in comparison with traditional refinement strategies which do not require the solution of the dual problem (18). To this end, we consider the (approximate) type II error indicator $\eta_\kappa^{(II)} = \|h R_h\|_{L_2(\kappa)} + \|h^{1/2} r_h\|_{L_2(\partial\kappa)}$ (cf. [18]). Throughout this section, we set $p = 1$ and $\hat{p} = 2$; additionally, for problems with a curved boundary Γ , we approximate Γ by a continuous piecewise quadratic polynomial function. We note that all computations are performed with the fixed fraction mesh refinement algorithm, with refinement and derefinement fractions set to 20 and 10%, respectively.

The system of nonlinear equations arising from (13) are solved using a damped Newton iteration method; the resulting linear iteration steps, together with the system of linear

equations arising from the dual problem, are solved by employing the GMRES method with a block Gauss–Seidel preconditioner. For a full discussion of this solution procedure, together with computational comparisons with pseudo-time-stepping schemes and other block preconditioners, we refer readers to [13].

Finally, we remark that for the numerical examples presented in Sections 5.1 and 5.3, precise values of the target functionals of interest are not known analytically; thereby, in each case, reference values are determined from the finest adaptive grid generated by employing the (approximate) type I error indicator $|\hat{\eta}_k^{(I)}|$.

5.1 Transonic Flow in a Converging–Diverging Nozzle

In this first example we consider the transonic flow in a converging–diverging nozzle. The computational domain is shown in Fig. 2; here, the upper and lower walls of the nozzle are given by the function g^\pm , respectively, where

$$g^\pm(x) = \begin{cases} \pm 1, & -2 \leq x \leq 0, \\ \pm(\cos(\pi x/2) + 3)/4, & 0 \leq x \leq 4, \\ \pm 1, & 4 \leq x \leq 8. \end{cases}$$

At the (subsonic) inflow, corresponding to $x = -2$, $-1 \leq y \leq 1$, we set the density $\rho = 1$, the pressure $p = 1$, and the Mach number $M = 0.3$; along $x = 8$, $-1 \leq y \leq 1$, we simply prescribe an outflow pressure condition $p = 2/3$ (cf. Brooksbanks [7]). The structure of the solution to this problem is as follows: the subsonic flow enters the computational domain from the left-hand side and accelerates as it enters the converging part of the nozzle, becoming sonic around the geometric throat of the nozzle. As the nozzle expands, the flow continues to accelerate before forming a shock, after which it becomes subsonic again (cf. Fig. 2).

Here, we take the functional of interest to be the value of the density in the supersonic region of the domain, just before the shock forms. More precisely, we choose $J(\cdot)$ to be the linear functional given by $J(\mathbf{u}) = \rho(3.25, 0.4)$; thereby, on the basis of a fine-grid computation, the true value of the functional is given by $J(\mathbf{u}) = 0.249695$.

In Table I, we demonstrate the performance of the adaptive algorithm with $C_\epsilon = 2/25$ and $\beta = 1/10$. Here, we show the number of elements and degrees of freedom (DOF) in $S_{h,1}$, the true error in the functional $J(\mathbf{u}) - J(\mathbf{u}_h)$, the computed error representation formula (29), the (approximate) *a posteriori* error bound (28), and their respective effectivity indices $\theta_1 = \hat{\mathcal{E}}_\Omega^{(I)} / (J(\mathbf{u}) - J(\mathbf{u}_h))$ and $\theta_2 = \hat{\mathcal{E}}_{|\Omega|}^{(I)} / |J(\mathbf{u}) - J(\mathbf{u}_h)|$. We see that initially on very coarse meshes the quality of the computed error representation formula $\hat{\mathcal{E}}_\Omega^{(I)}$ is very poor, in the sense that θ_1 is not close to one; however, as the mesh is refined, the effectivity index θ_1 approaches unity. Furthermore, we see that the type I *a posteriori* error bound $\hat{\mathcal{E}}_{|\Omega|}^{(I)}$ overestimates the true error in the computed functional by about an order of magnitude. We recall that $\mathcal{E}_{|\Omega|}^{(I)}$ was

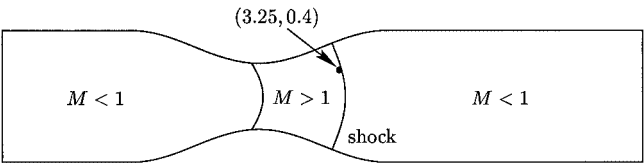


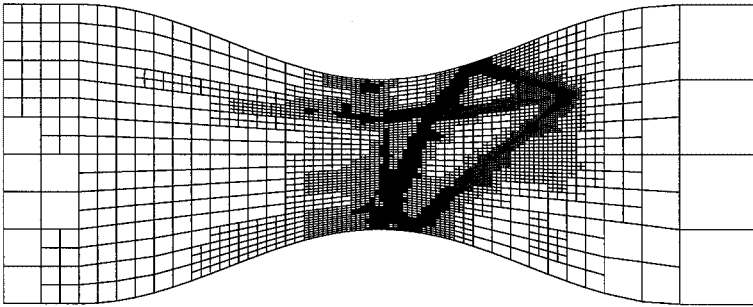
FIG. 2. Geometry for the converging–diverging nozzle problem; here, M denotes the Mach number.

TABLE I
Adaptive Algorithm for the Transonic Nozzle Problem

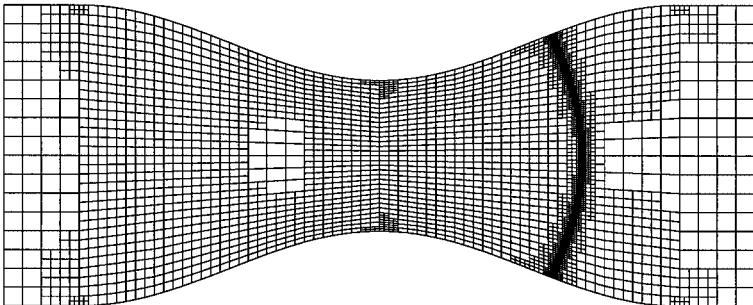
Elements	DOF	$J(\mathbf{u}) - J(\mathbf{u}_h)$	$\sum_{\kappa} \hat{\eta}_{\kappa}^{(I)}$	θ_1	$\sum_{\kappa} \hat{\eta}_{\kappa}^{(I)} $	θ_2
80	1,280	-2.357e-01	-1.667e-02	0.07	7.201e-02	0.31
143	2,288	-1.997e-01	-5.073e-02	0.25	2.101e-01	1.05
224	3,584	-5.983e-02	-7.678e-02	1.28	1.780e-01	2.98
350	5,600	3.754e-02	4.667e-02	1.24	9.503e-02	2.53
590	9,440	2.954e-02	1.772e-02	0.60	9.194e-02	3.11
926	14,816	1.663e-02	1.651e-02	0.99	5.547e-02	3.34
1,478	23,648	-1.851e-03	-2.128e-03	1.15	1.987e-02	10.73
2,462	39,392	2.256e-05	1.176e-05	0.52	2.540e-03	112.58
4,088	65,408	2.466e-05	2.492e-05	1.01	1.070e-03	43.41
6,719	107,504	1.136e-05	1.258e-05	1.11	6.287e-04	55.36
10,805	172,880	6.947e-06	7.169e-06	1.03	3.538e-04	50.92
17,588	281,408	3.102e-06	3.102e-06	1.00	2.112e-04	68.09

derived from the error representation formula by simply employing the triangle inequality; thereby, it is clear that any further bounding of $\mathcal{E}_{|\Omega|}^{(I)}$ performed *en route* to deriving a type II *a posteriori* error estimate will lead to a loss of sharpness of the computed error bound in the sense that the size of the resulting effectivity indices will be even larger.

In Fig. 3 we show the meshes generated using both the type I error indicator $|\hat{\eta}_{\kappa}^{(I)}|$ and the type II error indicator $\eta_{\kappa}^{(II)}$. From Fig. 3a, we see that there is virtually no refinement in



(a)



(b)

FIG. 3. Transonic nozzle problem. (a) Mesh constructed using the type I error indicator with 10,805 elements and 172,880 degrees of freedom ($|J(\mathbf{u}) - J(\mathbf{u}_h)| = 6.947 \times 10^{-6}$); (b) Mesh constructed using the type II error indicator with 21,353 elements and 341,648 degrees of freedom ($|J(\mathbf{u}) - J(\mathbf{u}_h)| = 2.841 \times 10^{-5}$).

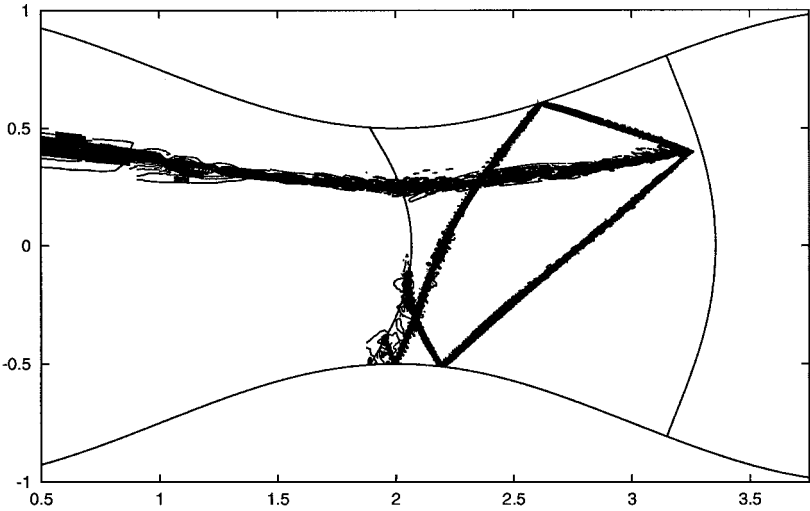


FIG. 4. Transonic nozzle problem. First component \hat{z}_1 of the dual solution for point evaluation of the density.

the region of the computational domain where the shock is located when $|\hat{\eta}_k^{(1)}|$ is employed. Indeed, most of the mesh refinement is concentrated in a series of one-dimensional lines upstream of the point of interest. This is due to the presence of the weighting terms involving the difference between the (approximated) dual solution $\hat{\mathbf{z}}$ and \mathbf{z}_h , which multiply the computable residual terms involving the numerical solution \mathbf{u}_h in the definition of the local error indicator $|\hat{\eta}_k^{(1)}|$ (cf. (20)) with \mathbf{z} replaced by $\hat{\mathbf{z}}$. Indeed, from Fig. 4, we see that the dual solution consists of a series of three “spikes” originating from the point of interest; here, we have only shown \hat{z}_1 , though the other components of the dual solution have a similar structure. More precisely, in this example, the dual solution is a Green function of the linearised adjoint compressible Euler equations driven by a delta function concentrated at the point of interest (cf. [25]). Thereby, within the supersonic region of the computational domain, the delta function leads to the generation of three spikes aligned with the three characteristic directions corresponding to the three eigenvalues \bar{v} and $\bar{v} \pm c$, where $\bar{v} = \sqrt{u^2 + v^2}$ denotes the velocity of the gas and $c = \sqrt{\gamma p / \rho}$ the speed of sound. We see that the middle characteristic \bar{v} , corresponding to mass transport, is carried upstream through the subsonic region to the inflow boundary located at $x = -2$. In contrast, the two characteristics corresponding to information transport due to sound waves are first reflected off the walls of the nozzle in the supersonic region but are then prevented from entering the subsonic region where these characteristics become complex. This corresponds to a change in type in the underlying system of partial differential equations; here, the steady compressible Euler equations change from hyperbolic in the supersonic region of the computational domain to elliptic in the subsonic region. In contrast, we see that when these weighting terms are neglected, the mesh produced using the type II error indicator is largely concentrated in the vicinity of the shock, with some further, almost uniform refinement within the nozzle itself (cf. Fig. 3b).

Finally, in Fig. 5, we compare the true error in the computed functional $J(\cdot)$ using the two mesh refinement strategies; here, we plot both the error versus the number of degrees of freedom in the finite element space $S_{h,p}$ and the error versus the computational effort. In both cases Fig. 5 clearly demonstrates the superiority of the type I *a posteriori* error indicator; on the final mesh the true error in the linear functional is over an order of magnitude smaller

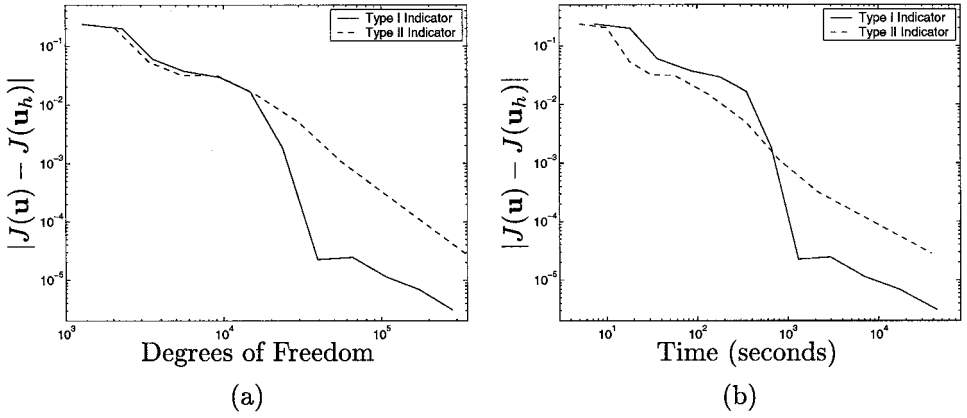


FIG. 5. Transonic nozzle problem. Convergence of $|J(\mathbf{u}) - J(\mathbf{u}_h)|$ using the type I and type II error indicators. (a) Error versus degrees of freedom; (b) error versus computational effort.

than $|J(\mathbf{u}) - J(\mathbf{u}_h)|$ computed on the sequence of meshes produced using $\eta_k^{(II)}$. This clearly indicates that a good numerical resolution of the shock in this example is irrelevant for the accurate approximation of the functional of interest. We remark that within the approximate type II error indicator $\eta_k^{(II)}$, we have formally set all the constants equal to one. Given that the fixed fraction strategy is employed, the absolute size of $\eta_k^{(II)}$ is insignificant: only the relative sizes of these quantities matter, which justifies setting all constants to unity. However, for error control purposes, the interpolation and stability constants arising within a type II *a posteriori* analysis of the error in the computed functional should also be included. In this case, the computational time involved in estimating the stability factor of the dual problem for the selected target functional should also be accounted for in Fig. 5b.

5.2. Subsonic Flow around a NACA0012 Airfoil

In this second example, we consider the subsonic flow around a NACA0012 airfoil; here, the upper and lower surfaces of the airfoil geometry are specified by the function g^\pm , respectively, where

$$g^\pm(s) = \pm 5 \times 0.12 \times (0.2969s^{1/2} - 0.126s - 0.3516s^2 + 0.2843s^3 - 0.1015s^4)$$

(cf. Fig. 6). We note that the chord length l of the airfoil is $l \approx 1.00893$; thereby, we write \hat{g} to denote the rescaling of g to yield an airfoil of unit (chord) length. The computational domain Ω is now defined to be an annulus with inner boundary \hat{g} and an outer boundary consisting of a circle with a radius of 10 units. On the outer boundary, we prescribe a Mach 0.5 flow at a zero angle of attack, with far-field density $\rho = 1$ and pressure $p = 1$. The solution to this problem consists of a strictly subsonic flow, symmetric about the x -axis (cf. Fig. 7). Given that this flow is smooth, no artificial viscosity is required; thereby, we set $C_\varepsilon = 0$.



FIG. 6. Profile of the NACA0012 airfoil.

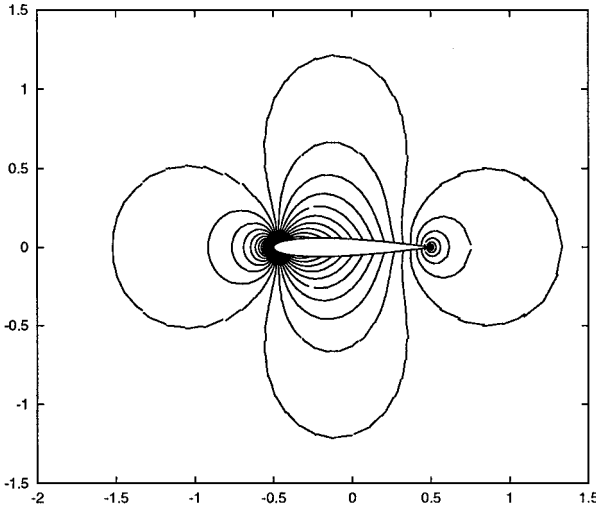


FIG. 7. Pressure isolines for the subsonic NACA0012 flow.

In this section we are interested in computing the drag and lift coefficients defined by

$$J_{\text{drag}}(\mathbf{u}) = \frac{2}{\bar{l}\bar{\rho}|\bar{\mathbf{v}}|2} \int_S (\psi_d \cdot \mathbf{n}) p \, ds, \quad J_{\text{lift}}(\mathbf{u}) = \frac{2}{\bar{l}\bar{\rho}|\bar{\mathbf{v}}|2} \int_S (\psi_l \cdot \mathbf{n}) p \, ds,$$

respectively. Here, S denotes the surface of the airfoil \hat{g} , $\bar{l} = 1$ is its chord length, $\bar{\mathbf{v}}$ and $\bar{\rho}$ denote the reference/free-stream velocity and density, respectively, and

$$\psi_d = \begin{pmatrix} \cos(\alpha) & -\sin(\alpha) \\ \sin(\alpha) & \cos(\alpha) \end{pmatrix} \begin{pmatrix} 1 \\ 0 \end{pmatrix}, \quad \psi_l = \begin{pmatrix} \cos(\alpha) & -\sin(\alpha) \\ \sin(\alpha) & \cos(\alpha) \end{pmatrix} \begin{pmatrix} 1 \\ 0 \end{pmatrix},$$

where α denotes the angle of attack. We note that since the pressure p is derived from the conserved variables $(\rho, \rho u, \rho v, pE)$ using the equation of state, both target functionals $J_{\text{drag}}(\cdot)$ and $J_{\text{lift}}(\cdot)$ are nonlinear. Given that the angle of attack $\alpha = 0$, the true value of both target functionals $J_{\text{drag}}(\cdot)$ and $J_{\text{lift}}(\cdot)$ is zero.

Let us first consider the case of estimating the drag on the surface of the airfoil, i.e., when $J(\cdot) \equiv J_{\text{drag}}(\cdot)$. To this end, in Table II we show the performance of our adaptive algorithm; here, we see that the quality of the computed error representation formula is extremely good, with $\theta_1 \approx 1$ even on relatively coarse meshes. Furthermore, the type I *a posteriori* error bound (28) is sharper for this smooth problem; here, $\hat{\mathcal{E}}_{|\Omega|}^{(1)}$ overestimates the true error in the computed functional by about a factor of 2–3.

The meshes produced using both the type I error indicator $|\hat{\eta}_{\mathbf{k}}^{(1)}|$ and the type II error indicator $\eta_{\mathbf{k}}^{(\text{II})}$ are shown in Fig. 8. Here, we see that both meshes are fairly similar in character, in the sense that most of the refinement is concentrated in the neighbourhood of the leading and trailing edges of the airfoil. However, we see that the mesh designed by the type I error indicator is also refined along the upper and lower surfaces of the airfoil. These extra regions of refinement are introduced as a result of the weighting terms present in the error indicator $|\hat{\eta}_{\mathbf{k}}^{(1)}|$ (cf. (20)). Indeed, in Fig. 9, we see that while there is a singularity in the dual solution at the leading edge of the airfoil, which is transported upstream along the characteristic with eigenvalue \bar{v} , $\hat{\mathbf{z}}_1$ also has large gradients around the whole of the

TABLE II

Subsonic NACA0012 Flow: Adaptive Algorithm for the Evaluation of the Drag Coefficient

Elements	DOF	$J(\mathbf{u}) - J(\mathbf{u}_h)$	$\sum_{\kappa} \hat{\eta}_{\kappa}^{(I)}$	θ_1	$\sum_{\kappa} \hat{\eta}_{\kappa}^{(I)} $	θ_2
39	624	-1.739e-02	-1.591e-02	0.91	2.906e-02	1.67
66	1,056	-6.041e-03	-3.070e-04	0.05	1.934e-02	3.20
111	1,776	-6.914e-03	-1.798e-03	0.26	2.491e-02	3.60
177	2,832	-5.542e-03	-3.427e-03	0.62	1.893e-02	3.42
279	4,464	-3.888e-03	-3.493e-03	0.90	1.018e-02	2.62
420	6,720	-1.357e-03	-1.303e-03	0.96	5.157e-03	3.80
678	10,848	-8.786e-04	-8.907e-04	1.01	2.417e-03	2.75
1,029	16,464	-5.926e-04	-6.901e-04	1.16	1.306e-03	2.20
1,605	25,680	-2.519e-04	-2.756e-04	1.09	5.574e-04	2.21
2,508	40,128	-1.234e-04	-1.333e-04	1.08	2.956e-04	2.39
3,972	63,552	-7.969e-05	-8.222e-05	1.03	1.976e-04	2.48

geometry. In Fig. 10 we compare the true error in the computed functional $J(\cdot)$ using the two mesh refinement strategies. First, we note that here the convergence of $|J(\mathbf{u}) - J(\mathbf{u}_h)|$ on the sequence of meshes produced with the type I error indicator is much “smoother” than on the meshes designed with the type II error indicator. Indeed, on finer meshes the error is even monotonic, allowing extrapolation of the value of the target functional in comparison to the “zigzag” convergence of $|J(\mathbf{u}) - J(\mathbf{u}_h)|$ on the meshes designed by $\eta_{\kappa}^{(II)}$. Again, as in the previous example, we clearly see that the type I *a posteriori* error indicators produce more economical meshes than when the traditional type II error indicator is employed, in the sense that $|J(\mathbf{u}) - J(\mathbf{u}_h)|$ is always smaller for a given number of degrees of freedom and almost always smaller for a given amount of computational effort.

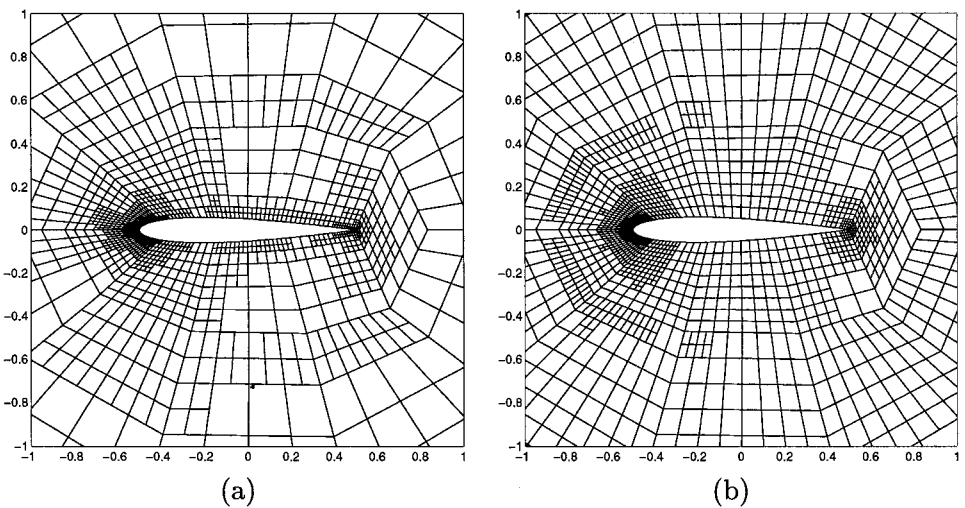


FIG. 8. Evaluation of the drag coefficient for the subsonic NACA0012 flow. (a) Mesh constructed using the type I error indicator with 2508 elements and 40,128 degrees of freedom ($|J(\mathbf{u}) - J(\mathbf{u}_h)| = 1.234 \times 10^{-4}$); (b) mesh constructed using the type II error indicator with 2634 elements and 42,144 degrees of freedom ($|J(\mathbf{u}) - J(\mathbf{u}_h)| = 5.856 \times 10^{-4}$).

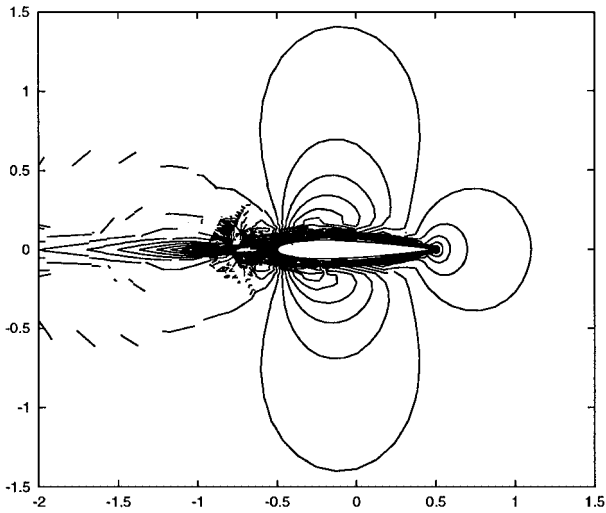


FIG. 9. Subsonic NACA0012 airfoil. First component \hat{z}_1 of the dual solution for the evaluation of the drag coefficient.

We end this section by considering the case when $J(\cdot) \equiv J_{\text{lift}}(\cdot)$. This is a relatively easy task; on a symmetric grid consisting of only 48 elements, the true error is $J(\mathbf{u}) - J(\mathbf{u}_h) = 1.332 \times 10^{-9}$, and the computed error representation formula is $\hat{\mathcal{E}}_{\Omega}^{(l)} = 2.1455 \times 10^{-9}$, giving rise to the effectivity index $\theta_1 = 1.61$.

5.3. Supersonic Flow around a BAC3-11 Airfoil

In this final example we study a supersonic flow around a BAC3-11 airfoil; this un-symmetric airfoil (see Fig. 11) was originally specified in the AGARD report AR-303. We consider a Mach 1.2 flow at an angle of attack $\alpha = 5^\circ$, with inflow density $\rho = 1$ and pressure $p = 1$. Throughout this section, we set the shock-capture parameters C_ϵ and β , appearing in (14), equal to $1/50$ and $1/10$, respectively.

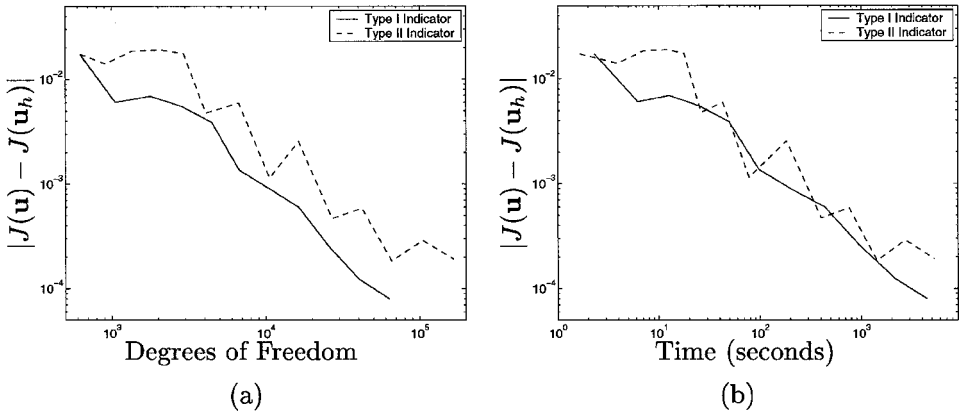


FIG. 10. Evaluation of the drag coefficient for the subsonic NACA0012 flow. Convergence of $|J(\mathbf{u}) - J(\mathbf{u}_h)|$ using the type I and type II error indicators. (a) Error versus degrees of freedom; (b) error versus computational effort.



FIG. 11. Profile of the BAC3-11 airfoil. Quantity of interest: pressure p at leading edge.

The structure of the solution to this problem includes two shocks: one located in front of the leading edge of the airfoil and one originating from the trailing edge (see Fig. 12a and also Fig. 13b, which shows a mesh that is refined at the position of the two shocks). Here, Fig. 12a shows the Mach 1 isolines of the solution; the Mach $M = 1$ isoline to the left of the airfoil indicates the position of the first shock. The $M = 1$ isolines that originate from the upper and lower surfaces of the airfoil represent the transonic lines of the flow. The flow left of the first shock is supersonic; it is simply the $M = 1.2$ flow prescribed on the inflow boundary of the computational domain. The flow in between the shock and the transonic lines is subsonic; we note that the leading edge of the airfoil is located within this subsonic part of the flow. Finally, the flow behind the transonic lines is supersonic again.

In this example we take the functional of interest to be the value of the pressure at the leading edge; i.e., $J(\mathbf{u}) = p(0, 0)$ (cf. Fig. 11). We note that, as in the case of estimating the drag and lift coefficients of a body immersed in an inviscid fluid (cf. Section 5.2), this functional is nonlinear, as it depends on the pressure. A computation on a fine grid gives a reference value of $J(\mathbf{u}) = 2.393$.

The structure of the dual solution $\hat{\mathbf{z}}$ corresponding to this point evaluation is displayed in Fig. 12b. This figure illustrates some principles of information transport in supersonic

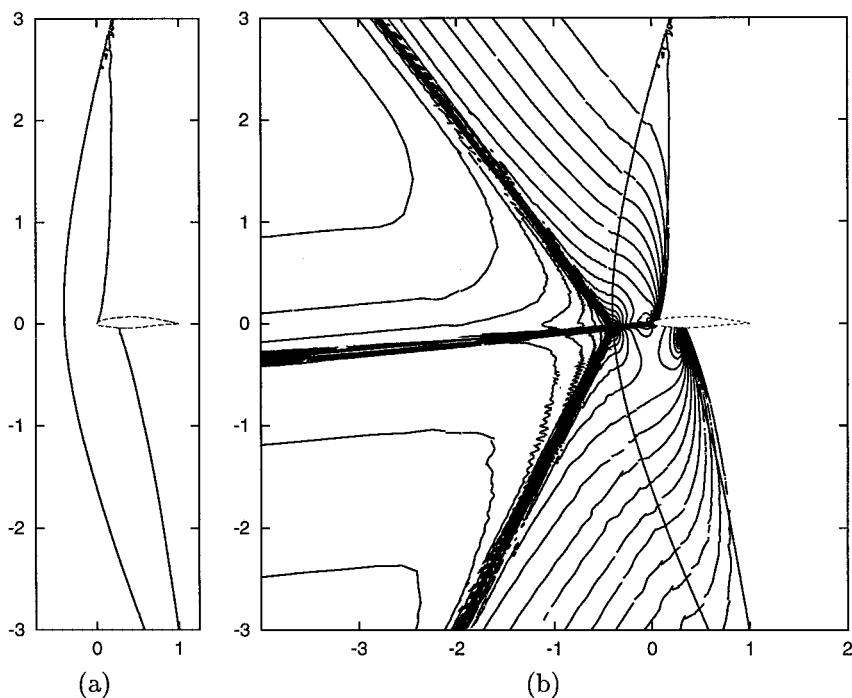


FIG. 12. Supersonic BAC3-11 flow. (a) Mach 1 isolines of the primal solution; (b) \hat{z}_1 isolines of dual solution and the Mach 1 isolines of the primal solution.

as well as in subsonic flow regions, as we saw in Sections 5.1 and 5.2. To the right-hand side of the transonic lines the dual solution is zero, as no information, either by material transport or by information transport due to sound waves, can enter the subsonic region from the supersonic one. Within the whole subsonic region the dual solution is nonzero, corresponding to the fact that sound waves can reach the point of evaluation from any point in the subsonic area and that all numerical errors which occur within this subsonic region can (even though possibly to a small portion) affect the value of the solution at the point of evaluation. Nevertheless, the dual solution in the subsonic region is concentrated in a thin spike; this spike originates from the point of evaluation and corresponds to the path of material transport and represents the main path of information transport. To the left of the airfoil, this spike crosses the shock and splits into three spikes while entering the supersonic region left of the shock. These spikes represent the characteristics corresponding to the three eigenvalues \bar{v} and $\bar{v} \pm c$. We recall that the characteristic corresponding to \bar{v} represents the path of material transport, which in this example is given by the line inclined at 5 degrees, whereas the characteristics corresponding to $\bar{v} \pm c$ represent the paths of information transport due to sound waves.

In Table III we show the performance of our adaptive algorithm. Here, we see that on very coarse meshes the quality of the computed error representation formula $\hat{\mathcal{E}}_{\Omega}^{(I)}$ is quite poor, in the sense that the effectivity index θ_1 is not close to one. However, ignoring the first few refinement steps, we see that θ_1 lies in the interval (0.94, 1.79). Moreover, we observe that the type I *a posteriori* estimate provides a reliable upper bound on the size of the error in the computed functional $J(\cdot)$.

In Fig. 13 we show the meshes produced using the type I and type II error indicators. Here, we see that the mesh constructed using $\eta_k^{(II)}$ is concentrated in the neighbourhood of the two shocks. In contrast, the mesh produced using the type I error indicator $|\hat{\eta}_k^{(I)}|$ only refines the mesh in the vicinity of the point of evaluation and the part of the shock where the spike of the dual solution, i.e., where the main part of information, crosses the shock. The other parts of the shock are not resolved, as the numerical error in these regions only has a small affect on the accuracy of the solution at the point of evaluation. Also, there is no refinement in the vicinity of the shock emanating from the trailing edge of the airfoil; thereby, this shock is not well resolved at all. Nevertheless the solution at the leading edge of the airfoil is not

TABLE III
Supersonic BAC3-11 Flow: Adaptive Algorithm for the Point Evaluation
of the Pressure at the Leading Edge

Elements	DOF	$J(\mathbf{u}) - J(\mathbf{u}_h)$	$\sum_{\kappa} \hat{\eta}_{\kappa}^{(I)}$	θ_1	$\sum_{\kappa} \hat{\eta}_{\kappa}^{(I)} $	θ_2
39	624	3.188e-01	2.773e-01	0.87	4.288e-01	1.35
63	1,008	2.313e-01	-1.501e-02	-0.06	2.003e-01	0.87
114	1,824	2.069e-01	-7.275e-02	0.35	3.498e-01	1.69
192	3,072	7.398e-02	5.404e-02	0.73	2.680e-01	3.62
348	5,568	6.425e-02	2.695e-02	0.42	2.120e-01	3.30
609	9,744	2.876e-02	1.389e-02	0.48	1.839e-01	6.39
1,065	17,040	5.066e-03	7.602e-03	1.50	1.171e-01	23.11
1,803	28,848	3.402e-03	2.868e-03	0.94	1.028e-01	33.78
3,045	48,720	1.561e-03	2.801e-03	1.79	1.067e-01	68.39
5,643	90,288	5.790e-04	5.790e-04	1.00	5.551e-02	95.88

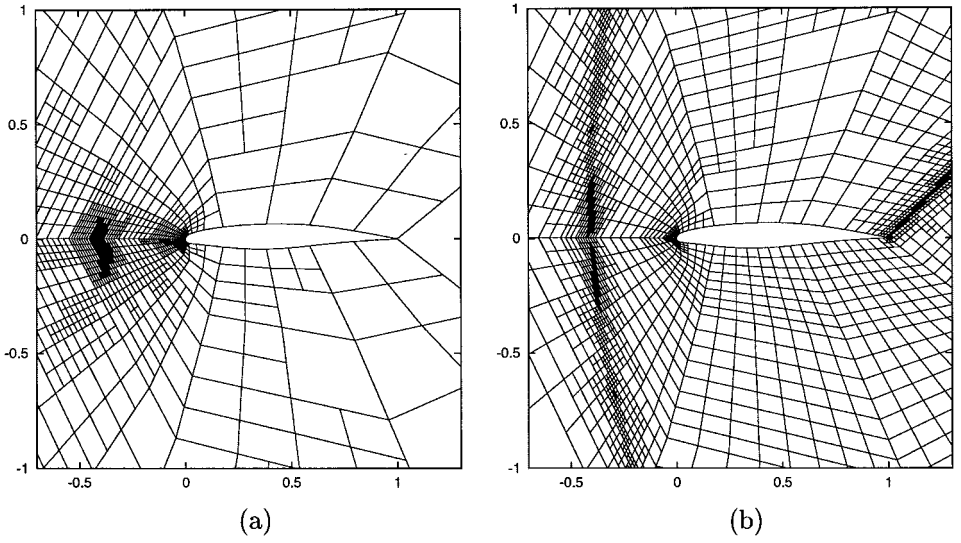


FIG. 13. Supersonic BAC3-11 flow. (a) Mesh constructed using the type I error indicator with 1803 elements and 28,848 degrees of freedom ($|J(\mathbf{u}) - J(\mathbf{u}_h)| = 3.042 \times 10^{-3}$); (b) mesh constructed using the type II error indicator with 13,719 elements and 219,504 degrees of freedom ($|J(\mathbf{u}) - J(\mathbf{u}_h)| = 3.542 \times 10^{-2}$).

affected by this, as no information is transported upstream from the trailing edge, located in a supersonic part of the flow, to the leading edge, located in the subsonic region. As in the previous examples, we see that the adaptively refined meshes generated by employing the type I error indicator $|\hat{\eta}_k^{(I)}|$ are much more economical than those produced using the traditional type II error indicator $\eta_k^{(II)}$. Indeed, in Fig. 14 we clearly observe the superiority of the former error indicator; on the final mesh the true error in the computed functional is over two orders of magnitude smaller when the type I error indicator is employed.

Motivated by the structure of the mesh generated by the type I indicator, we also consider the performance of an alternative type II error indicator based on a modification of $\eta_k^{(II)}$, whereby only elements in a neighbourhood of a region upstream of the point of interest are

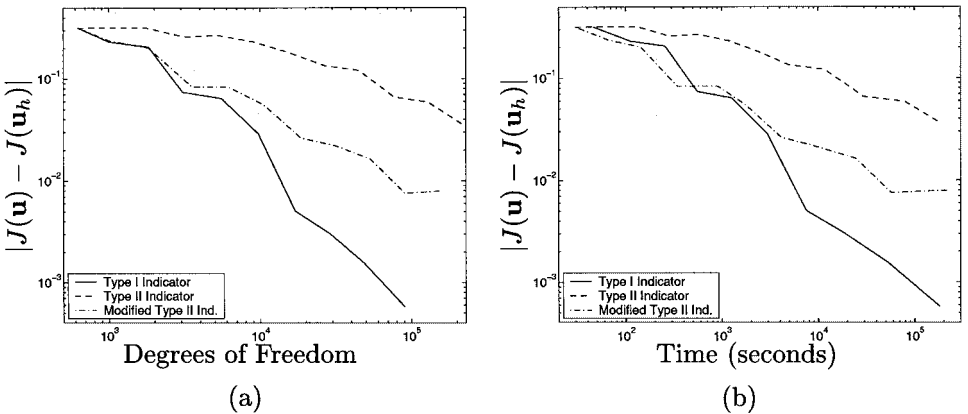


FIG. 14. Supersonic BAC3-11 flow. Convergence of $|J(\mathbf{u}) - J(\mathbf{u}_h)|$ using the type I and type II error indicators. (a) Error versus degrees of freedom; (b) error versus computational effort.

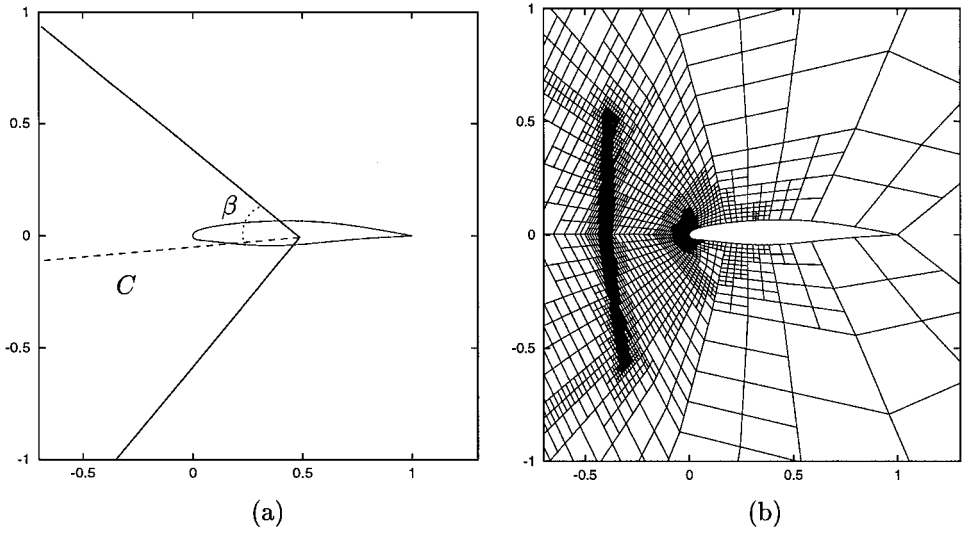


FIG. 15. Supersonic BAC3-11 flow. (a) Cone C : domain where the modified type II error indicator is active; (b) mesh constructed using the modified type II error indicator with 9516 elements and 152,256 degrees of freedom ($|J(\mathbf{u}) - J(\mathbf{u}_h)| = 7.924 \times 10^{-3}$).

marked for refinement. More precisely, we write C to denote the cone depicted in Fig. 15a with apex half angle β , located in the centre of the airfoil, with symmetry axes inclined at $\alpha = 5^\circ$, according to the direction of the inflow. We define the modified type II indicator $\eta_{\kappa}^{(\text{II},c)}$ as follows:

$$\eta_{\kappa}^{(\text{II},c)} = \begin{cases} \eta_{\kappa}^{(\text{II})}, & \text{if } \text{centroid}(\kappa) \in C, \\ 0, & \text{otherwise.} \end{cases}$$

This modification takes into account the fact that we are not interested in the flow field in the whole domain, but only in the point value of the pressure at the leading edge. Thereby, adaptive mesh refinement is inhibited in the region downstream of the airfoil, including the neighbourhood of the shock emanating from the trailing edge. Furthermore, refinement of the shock in front of the leading edge of the airfoil is prevented in regions that are placed too far above or below the airfoil, since a low resolution of this shock in these areas is believed to not significantly degrade the accuracy of the pressure value at the leading edge (cf. Fig. 13a). In Fig. 15b we show the mesh produced by employing $\eta_{\kappa}^{(\text{II},c)}$ with $\beta = 45^\circ$.

From Fig. 14 we see that the modified type II indicator produces meshes that are much more efficient for computing the value of the pressure at the leading edge of the airfoil in comparison to the (unmodified) type II indicator $\eta_{\kappa}^{(\text{II})}$. Nevertheless the meshes produced employing the type I indicators are even more efficient than those designed by $\eta_{\kappa}^{(\text{II},c)}$; on the final mesh the true error in the computed functional is over an order of magnitude smaller when the type I indicator is employed. We note that the chosen shape and size of the subdomain C and the resulting modified indicator only represents an “attempt” to find a reasonable modification of the type II indicator $\eta_{\kappa}^{(\text{II})}$ that is capable of efficiently computing the pressure at the leading edge of the airfoil and to provide a “fair” comparison with the goal-oriented type I indicator $|\hat{\gamma}_{\kappa}^{(\text{I})}|$. Indeed, the value of the angle β may be chosen differently, though *a priori* it is unclear which parts of the shock in front of the leading

edge of the airfoil will influence the target functional. The angle β should not be chosen too small, as otherwise the lack of resolution of the shock in front of the leading edge of the airfoil will impact on the computed value of the pressure at the point of interest; on the other hand choosing β too large may lead to overrefinement. In contrast, the type I error indicator provides all the necessary information to decide which regions of the shock should be refined, and to what extent.

6. CONCLUDING REMARKS

In this article we have applied the recently developed approach of weighted *a posteriori* error estimation for discontinuous Galerkin finite element methods to the discretisation of physically relevant problems arising in inviscid compressible fluid flows governed by the Euler equations of gas dynamics. Indeed, here weighted or type I (cf. [18]) *a posteriori* error bounds have been employed for the design of economical adaptive finite element algorithms capable of delivering sharp error estimation for general linear and nonlinear target functionals of the solution. Numerical experiments have been presented to illustrate both the quality of the approximate error representation formula and the resulting type I *a posteriori* error bound, when the (approximate) dual problem is approximated numerically. In all cases, our weighted *a posteriori* estimates provide sharp upper bounds on the size of the error in the computed target functional of physical interest. Moreover, comparisons with traditional type II error indicators which stem from type II *a posteriori* error bounds have clearly demonstrated the superiority of exploiting weighted *a posteriori* error indicators to guide adaptive mesh refinement; in all examples, the error in the computed target functional is significantly smaller for a given number of degrees of freedom and a given amount of computational effort when the proposed error indicator is employed.

ACKNOWLEDGMENTS

Ralf Hartmann acknowledges the financial support of the DFG Priority Research Program and the SFB 359 at the IWR, University of Heidelberg. Paul Houston acknowledges the financial support of the EPSRC (Grant GR/N24230). Part of this work was performed using the University of Leicester Mathematical Modelling Centre's supercomputer, which was purchased through the EPSRC strategic equipment initiative.

REFERENCES

1. M. Ainsworth and J. T. Oden, *A Posteriori Error Estimation in Finite Element Analysis*, Series in Computational and Applied Mathematics (Elsevier, Amsterdam/New York, 1996).
2. W. Bangerth and R. Rannacher, Adaptive finite element approximation of the acoustic wave equation: Error estimation and mesh adaptation, *East-West J. Numer. Math.* **7**(4), 263 (1999).
3. T. J. Barth and M. G. Larson, A posteriori error estimates for higher order Godunov finite volume methods on unstructured meshes, in *Finite Volumes for Complex Applications III*, edited by R. Herbin and D. Kroner Proceedings of FVCA, Porquerolles, France, June 2002 (HERMES Science Publishing Ltd., London, 2002), pp. 41–63.
4. F. Bassi and S. Rebay, High-order accurate discontinuous finite element solution of the 2D Euler equations, *J. Comput. Phys.* **138**, 251 (1997).
5. R. Becker and R. Rannacher, A feed-back approach to error control in finite element methods: Basic analysis and examples, *East-West J. Numer. Math.* **4**, 237 (1996).

6. R. Becker and R. Rannacher, An optimal control approach to a-posteriori error estimation in finite element methods, *Acta Numer.* **10**, 1 (2001).
7. E. Brooksbanks, *A Numerical Investigation of Time Resolved Flows Around Turbine Blades*, Ph.D. thesis (University of Leicester, 2002).
8. B. Cockburn, G. E. Karniadakis, and C.-W. Shu, The development of discontinuous Galerkin methods, in *Discontinuous Galerkin Methods*, edited by B. Cockburn, G. Karniadakis, and C.-W. Shu, Lecture Notes in Computational Science and Engineering (Springer-Verlag, Berlin, 2000), Vol. 11, p. 3.
9. K. Eriksson, D. Estep, P. Hansbo, and C. Johnson, Introduction to adaptive methods for differential equations, *Acta Numer.* 105 (1995).
10. M. B. Giles and E. Süli, Adjoint methods for PDEs: a posteriori error analysis and postprocessing by duality, *Acta Numer.* **11**, 145 (2002).
11. P. Hansbo and C. Johnson, *Streamline Diffusion Finite Element Methods for Fluid Flow* (von Karman Institute Lectures, 1995).
12. K. Harriman, *Applications of Adaptive Finite Element Methods to Problems in Electrochemistry*, D.Phil. thesis (University of Oxford, 2000).
13. R. Hartmann, *Adaptive Finite Element Methods for the Compressible Euler Equations*, Ph.D. thesis (University of Heidelberg, 2002).
14. R. Hartmann and P. Houston, Adaptive discontinuous Galerkin finite element methods for nonlinear hyperbolic conservation laws, *SIAM J. Sci. Comput.*, in press.
15. R. Hartmann and P. Houston, *Goal-Oriented A Posteriori Error Estimation for Multiple Target Functionals*, Technical Report 2002/32 (University of Leicester, 2002).
16. P. Houston, R. Hartmann, and E. Süli, Adaptive discontinuous Galerkin finite element methods for compressible fluid flows, in *Numerical Methods for Fluid Dynamics VII*, edited by M. Baines, Numerical Methods for Fluid Dynamics (Institute for Computational Fluid Dynamics, Oxford, 2001), Vol. 8, p. 347.
17. P. Houston, R. Rannacher, and E. Süli, A posteriori error analysis for stabilised finite element approximations of transport problems, *Comput. Methods Appl. Mech. Eng.* **190**(11–12), 1483 (2000).
18. P. Houston and E. Süli, hp-Adaptive discontinuous Galerkin finite element methods for first-order hyperbolic problems, *SIAM J. Sci. Comput.* **23**(4), 1225 (2001).
19. J. Jaffre, C. Johnson, and A. Szepessy, Convergence of the discontinuous Galerkin finite element method for hyperbolic conservation laws, *Math. Models Methods Appl. Sci.* **5**(3), 367 (1995).
20. D. Kröner, *Numerical Schemes for Conservation Laws* (Wiley-Teubner, New York, 1997).
21. M. G. Larson and T. J. Barth, A posteriori error estimation for adaptive discontinuous Galerkin approximations of hyperbolic systems, in *Discontinuous Galerkin Methods*, edited by B. Cockburn, G. Karniadakis, and C.-W. Shu, Lecture Notes in Computational Science and Engineering (Springer-Verlag, Berlin, 2000), Vol. 11, p. 363.
22. J. T. Oden and S. Prudhomme, On goal-oriented error estimation for elliptic problems: Application to control of pointwise errors, *Comput. Methods Appl. Mech. Eng.* **176**, 313 (1999).
23. M. Paraschivoiu, J. Peraire, and A. Patera, A posteriori finite element bounds for linear functional outputs of elliptic partial differential equations, *Comput. Methods Appl. Mech. Eng.* **150**, 289 (1997).
24. R. Rannacher, Adaptive finite element methods, in *Proc. NATO-Summer School, Error Control and Adaptivity in Scientific Computing*, edited by H. Bulgak and C. Zenger (Kluwer Academic, Dordrecht/Norwell, MA, 1998), p. 247.
25. E. Süli and P. Houston, Adaptive finite element approximation of hyperbolic problems, in *Error Estimation and Adaptive Discretization Methods in Computational Fluid Dynamics*, edited by T. Barth and H. Deconinck, Lecture Notes in Computational Science and Engineering (Springer-Verlag, Berlin, 2002), Vol. 25, p. 269.
26. B. Szabó and I. Babuška, *Finite Element Analysis* (Wiley, New York, 1991).
27. D. A. Venditti and D. L. Darmofal, Grid adaptation for functional outputs: Application to two-dimensional inviscid flows, *J. Comput. Phys.* **176**(1), 40 (2002).
28. R. Verfürth, *A Review of A Posteriori Error Estimation and Adaptive Mesh-Refinement Techniques* (Teubner, Stuttgart, 1996).